

# Effects of Grain Boundary Misorientation and Chromium Segregation on Corrosion of CoCrMo Alloys

Alex Lin,\* Emily E. Hoffman,\* and Laurence D. Marks<sup>‡,\*</sup>

## ABSTRACT

*The influence of grain boundary interfacial energy on the structure of carbides and the local segregation of chromium were investigated at the nanoscale for coincident site lattice boundaries in a CoCrMo alloy. Grain boundaries of varying degrees of misorientation were examined by optical profilometry and transmission electron microscopy, and samples of the grain boundary precipitates were analyzed with energy dispersive x-ray spectroscopy. Low- $\Sigma$  coincident site lattice boundaries were found to have both fewer carbide precipitates and smaller degrees of sensitization, and are more resistant to intergranular attack. Similar to general high-angle boundaries in this material, the combination of chromium depletion and the grain boundary energy acts as the initiator of corrosion. After initiation, crevice corrosion enlarges the initial site of the attack.*

**KEY WORDS:** chromium, coincident site lattice, precipitation, sensitization, transmission electron microscopy

## INTRODUCTION

Orthopedic replacements for hips and knees are some of the most successful procedures for patients with severe osteoarthritis and rheumatoid arthritis. Currently, more than 300,000 total hip replacement operations are performed annually in the United States,<sup>1</sup> and this number is predicted to reach

1,800,000 by 2050.<sup>2</sup> Metal-on-metal (MoM) replacements made of cobalt chromium molybdenum alloys (CoCrMo) have attracted interest as an alternative to metal-on-polyethylene (MoP) implants because of their excellent mechanical properties, superior wear and corrosion resistance, longer service duration, and reduced inflammation response.<sup>3-4</sup> CoCrMo alloys, however, corrode at several micrometers per year, which can lead to damaging nanoparticle debris and ion release.<sup>5-8</sup> Thus, even though the overall corrosion rate is low, adverse side effects remain a challenge. Considering the millions of MoM hip replacements currently in use worldwide, a better understanding of the processes of corrosion in CoCrMo biomedical alloys is needed.

The dominant corrosion protection in all CoCrMo alloys is a thin film of chromium oxide. As this alloy corrodes, the mass loss of material is not constant; there is often preferential corrosion at grain boundaries, carbide phases, and defects. This focused corrosion is often classified as “grain boundary sensitization,” and for alloys that include chromium, local sensitization is explained as a localized reduction of chromium.<sup>9-11</sup> Sensitization has been extensively studied in stainless steel, with studies dating back to the 1930s.<sup>9</sup> Most notably, Stawstrom, et al., reported that a 13 at% minimum Cr concentration is the threshold value to prevent sensitization.<sup>12</sup> More recent studies by Bruemmer and Charlot,<sup>13</sup> and Pande, et al.,<sup>14</sup> clarified how Cr depletion occurs at the grain boundaries via the growth of nanoscale carbide precipitates. Bruemmer, et al.,<sup>15</sup> extensively studied Cr depletion zones of stainless steels using analytical transmission

Submitted for publication: August 18, 2016. Revised and accepted: November 17, 2016. Preprint available online: November 17, 2016. <http://dx.doi.org/10.5006/2233>.

<sup>‡</sup> Corresponding author. E-mail: l-marks@northwestern.edu.

\* Department of Materials Science and Engineering, Northwestern University, 2220 Campus Drive, Evanston, IL 60208.

electron microscopy (TEM), and showed that no carbides were found and cracking was limited when the Cr concentration exceeded 16.5 at% at the grain boundary. For a full discussion of sensitization, see the "Grain Boundary Sensitization" literature review section in Hoffman, et al.<sup>16</sup>

Microscale grain boundary sensitization was shown to affect corrosion in biomedical CoCrMo alloys. For high-carbon CoCrMo alloys, Montero-Ocampo and Martinez<sup>17</sup> showed that a large number of carbide precipitates depleted the matrix in Cr and Mo at grain boundaries to form  $M_{23}C_6$  carbides ( $M = Cr, Mo, Co$ ). Liao, et al.,<sup>18</sup> demonstrated with precession electron diffraction and high-resolution energy dispersive x-ray spectroscopy (EDS) that  $M_{23}C_6$  and  $M_6C$  carbides were present in annealed CoCrMo alloys. Bettini, et al.,<sup>19</sup> characterized microscale carbides in CoCrMo and observed increased corrosion at the Cr depletion areas. These CoCrMo carbide and sensitization studies were mainly confined to the microscale and did not consider the full combination of heat treatment, grain boundary type, corrosion, and nanoscale chemical analysis.

The local Cr depletion varies with type of grain boundary; it is well established that many properties such as corrosion susceptibility, mechanical strength, and precipitate formation are connected to the grain boundary structure and interfacial energy.<sup>20-24</sup> In general, grain boundary structure is quantified using the coincidence site lattice (CSL) model, where grain boundaries can be classified as having repeating coincident lattice points along the boundary. The degree of coincidence can be described by a  $\Sigma$ -value, which is the ratio of coincident lattice site area to the 2D crystal unit cell area. Low- $\Sigma$  grain boundaries have, in general, low interfacial energies, although the  $\Sigma$ -value and the interfacial energy are not linearly related, i.e.,  $\Sigma 25$  has a smaller interfacial energy than  $\Sigma 13$  in CoCrMo alloys.

For face-centered cubic (fcc) metals such as stainless steels and Ni alloys, CSL boundaries with  $\Sigma \leq 29$  are considered "geometrically special" and are less susceptible to intergranular corrosion.<sup>25</sup> The influence of grain boundary structure on sensitization and subsequent intergranular corrosion was studied by Palumbo, et al., for Ni alloys.<sup>21</sup> Geometrically special CSL boundaries have been found to inhibit the depletion of soluble Cr in the vicinity of the grain boundary and have enhanced corrosion resistance.<sup>22</sup> The size and spacing of the intergranular  $M_{23}C_6$  carbides in Ni alloys were dependent upon the characteristics of the grain boundary. Smaller carbides were found at  $\Sigma 3$  CSL grain boundaries, and larger carbides were found at higher  $\Sigma$  grain boundaries.<sup>26</sup> Carbide precipitation was influenced by CSL  $\Sigma$  and grain boundary interfacial energy; however, this relationship is still not clear in most alloys.

The relationship between CSL and intergranular corrosion was characterized by Panigrahi, et al.,<sup>27</sup>

who examined the corrosion susceptibility of CoCrMo alloys for various annealing temperatures and times. Based on the grain boundaries observed in the study, 90% of the grain boundaries with reciprocal lattice coincidence  $\Sigma 11$  or lower were completely immune to the in vitro electrochemical corrosion process. Hoffman, et al.,<sup>16</sup> established a model that compared corrosion susceptibility to grain boundary carbides and the Co and Cr contents at the boundaries by examination of high-energy, high- $\Sigma$  boundaries. It was demonstrated that CoCrMo alloys had nanoscale carbide precipitates accompanied by Cr depletion zones along grain boundaries, similar to observations of stainless steel. Additionally, the levels of Cr depletion at completely immune CSL boundaries were compared with the Cr depletion at completely corroded non-CSL boundaries. Larger precipitates and larger Cr depletion were found at high-energy boundaries, showing that Cr depletion at the interface can indicate corrosion susceptibility.

This study looks beyond the high-energy boundaries previously analyzed to the intermediate regime of lower energy boundaries that do corrode. By analyzing the morphology near the boundaries, grain boundary properties were connected to local corrosion susceptibility. High-resolution TEM and EDS revealed the chemical compositions at the boundaries. Crevice depth measurements, collected from white light interferometry, quantified corrosion susceptibility across grain boundaries and indicated that deeper corrosion crevices are linked to larger Cr depletion, suggesting that higher energy boundaries have higher likelihood of corroding more severely.

## METHODS

### Sample Preparation

A high-carbon wrought CoCrMo alloy, in accordance to ASTM F1537-08, was annealed in an air furnace for 24 h at 1,230°C and quenched in water. The alloy composition is given in Table 1. This heat treatment was chosen as it was most successful in reducing the bulk corrosion rate, localizing corrosion to grain boundaries, and optimizing the in vivo performance of the alloy. The solution-annealed CoCrMo sample was then ground, polished to a mirror finish ( $R_a \leq 10$  nm), and then electrochemically corroded according to the procedures used by Panigrahi, et al.<sup>27</sup> To summarize the corrosion conditions, the CoCrMo alloy sample was electrochemically corroded in a four-chamber corrosion cell. The sample was

**TABLE 1**  
*High-Carbon CoCrMo Alloy Composition*

at%	Co	Cr	Mo	C	Si	Mn	Ni	Fe
ASTM F1537-08	Balance	30.3	3.6	1.14	1.34	0.73	0.17	0.14

incorporated into the cell as the working electrode with a graphite counter electrode and a saturated calomel electrode reference electrode, all connected to a potentiostat. The cell was filled with 10 mL of bovine calf serum, containing a protein content of 30 g/L. The solution was buffered to a pH of 7.4 and the cell was placed in a hot water bath at 37°C in order to simulate human physiological conditions.

Standard electrochemical corrosion procedures were followed. The tests began with a potentiostatic test, where a constant potential of  $-0.9$  V was applied to remove the passive film and proteins that may have adsorbed on the metallic surface, followed by an electrochemical impedance spectroscopy (EIS) test. The EIS measurements were performed at frequencies from 100 kHz down to 10 mHz with an AC sine wave amplitude of 10 mV applied at the open-circuit potential. A cyclic polarization test was then performed to corrode the sample and measure the current at each applied potential. The samples were polarized from  $-0.8$  V to 1.8 V at a scan rate of 2 mV/s and then reversed back to  $-0.8$  V at the same rate. Using the corrosion current from Panigrahi, et al.'s results<sup>27</sup> and Faraday's equation, the dissolution rate was calculated to be 2.98  $\mu\text{m}/\text{y}$  and assumed to be uniform.

### Scanning Electron Microscopy

Scanning electron microscopy (SEM) characterization was performed on the FEI Quanta ESEM<sup>†</sup> operating at an accelerating voltage of 30 kV. Various regions of the electrochemically corroded CoCrMo surface were imaged at magnification levels between 300 $\times$  and 600 $\times$ . An Oxford<sup>†</sup> electron backscatter diffraction (EBSD) detector was then used to perform orientation image mapping (OIM) by collecting EBSD patterns of individual grains. A step size of 0.6  $\mu\text{m}$  was used, as it provided sufficient precision for obtaining crystallographic misorientation data with OIM. The acquired EBSD patterns were indexed using the commercially available EBSD processing software. Using the Oxford Tango<sup>†</sup> post-processing software, noise reduction was performed in order to minimize artifacts caused by surface roughness. Additionally, the misorientation of relevant grain boundaries was determined. The Brandon criterion<sup>28</sup> was used to classify the  $\Sigma$ -value, which is the ratio of coincident lattice sites to the 2D crystal unit cell area, of each identified CSL grain boundary.

### White Light Interferometry

Three-dimensional profilometry on a Bruker Contour GT-K<sup>†</sup> 3D optical microscope equipped with a Mirau interferometer objective lens was used to quantitatively determine the corrosion susceptibility by measuring the topography of various boundaries. In principle, the white light interferometer had a lateral

resolution limited by the wavelength of light. The z-axis resolution was limited by the sensitivity of the light intensity detector, and as a result, resolutions of the order of 10 nm were readily achieved. As previously reported in Hoffman, et al.,<sup>16</sup> this technique was used to characterize the widths and depths of the crevices associated with the corroded grain boundaries. A total of 25 boundaries, 13 CSL boundaries, and 12 non-CSL boundaries of varying corrosion susceptibility were measured. Two-dimensional projections of approximately 250  $\mu\text{m}$  by 300  $\mu\text{m}$  were acquired in order to record the profile of the corroded surface, and 15 to 20 depth and width scans were collected along each individual grain boundary. While measuring the depth of a crevice, the width was simultaneously acquired by measuring the distance between the two edges of the crevice. Reconstruction, specimen visualization, and measurements were performed using the Bruker Vision64 Analysis Software<sup>†</sup>. The means of the depth and width measurements, as well as the range to the 95% confidence level, were then computed.

### Focused Ion Beam

For further nanoscale analysis, TEM lamellae of CSL grain boundaries within the annealed CoCrMo alloy were produced in a dual-beam FEI Helios Nanolab<sup>†</sup> focused ion beam (FIB) system. The CSL boundary of interest, identified from the EBSD OIM data, was milled out with focused ion beam operating at 30 kV from 9.2 nA to 48 nA. The boundary cross section was then transferred to a TEM grid and thinned to an electron-transparent TEM sample. The final CoCrMo lamellae spanned 3  $\mu\text{m}$  to 4  $\mu\text{m}$  on either side of the boundary and reached 4  $\mu\text{m}$  deep below the bulk surface. Eight asymmetrically corroded CSL boundaries and two completely immune CSL boundaries were prepared into TEM lamellae samples.

### Transmission Electron Microscopy

TEM imaging and elemental analysis of grain boundaries were performed using a combination of TEMs including the Hitachi H-8100<sup>†</sup>, JEOL 2100F<sup>†</sup>, and JEOL ARM200-CF<sup>†</sup>, all operating at 200 kV. Bright field (BF) images, dark field (DF) images, and electron diffraction patterns were acquired on the H-8100<sup>†</sup> from eight corroded CSL boundaries and two immune CSL boundaries. Annular dark field (ADF) imaging and high-angle annular dark field (HAADF) imaging were performed on the 2100F<sup>†</sup> and ARM200-CF<sup>†</sup>, respectively. Analytical data including EDS mapping and line profiles were collected in scanning transmission electron microscopy (STEM) mode using an Oxford<sup>†</sup> windowless detector. The EDS data was then processed by the Oxford AZtecTEM<sup>†</sup> EDS software. In order to characterize nanoscale grain boundary carbide precipitates and Cr depletion zones at CSL boundaries, five selected CSL boundaries of varying corrosion susceptibility were analyzed with HAADF imaging.

<sup>†</sup> Trade name.

EDS mapping was performed on sections of individual boundaries and chemical quantification data were probed from key sites within the maps. On average, six EDS maps were collected from each CSL boundary and five to eight sites were probed from each EDS map.

## RESULTS

### Grain Boundary Misorientation

SEM imaging in combination with OIM analysis indicated that preferential intergranular corrosion had occurred, shown in Figures 1(a) through (c). The OIM mapping in Figure 1(c) labeled which boundaries were twin, CSL, or regular high-angle boundaries. Highly ordered twin boundaries were completely immune to corrosion attack, while high-energy grain boundaries with fewer coincident lattice points were more susceptible to corrosion.

SEM image analysis further showed that there were three distinct types of boundaries that corroded: Types I, II, and III. Type I corresponds to those which showed minimal to no corrosion, less than 0.4  $\mu\text{m}$  deep if at all. Types II and III showed definite corrosion. From analysis of the OIM data, Type I boundaries are twins or have a CSL value of  $\Sigma 11$  or smaller, whereas Type II were larger. This was determined to be a

threshold for corrosion resistance in a previous CoCrMo alloy study,<sup>27</sup> and confirmed in this data. Types II and III boundaries both corroded, yet with different profile shapes and to different degrees. Type II boundaries were asymmetric, indicating that these intermediate misorientations, such as  $\Sigma 17$  and  $\Sigma 25$ , were more resistant to corrosion attack in comparison to general high-angle grain boundaries. Out of 96 non-twin CSL boundaries, 57 of them corroded less than 1.0  $\mu\text{m}$ . These boundaries were classified as Type II boundaries. Beyond  $\Sigma 35$ , corrosion depths of greater than 1.0  $\mu\text{m}$  were observed, similar to the corroded general boundaries. Based upon this data, the threshold between Types II and III was the CSL value  $\Sigma 35$ . It should be noted that the CSL threshold level that corresponds to general high-angle boundaries is not completely fixed, and can vary with material. Representative example boundary morphologies of each type are shown in Figure 2.

With the CSL data from the OIM mapping, the same grain boundaries were measured with 3D profilometry. Figures 3(a) and (b) show a representative profilometry scan and Figures 3(c) through (e) show the extracted 2D boundary profile scans for each boundary type. The depth profiles of the different classes of the boundaries illustrate the distinction between them. In

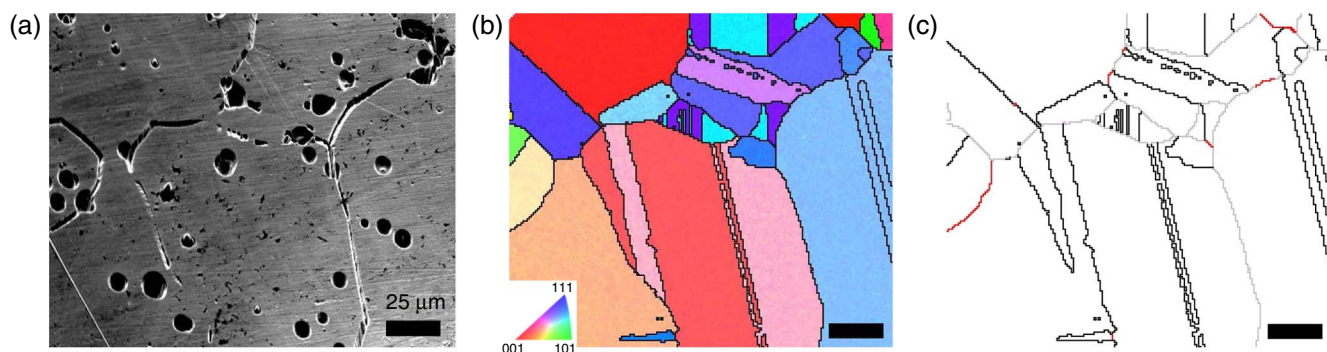


**FIGURE 1.** (a) SEM image and (b) its corresponding EBSD map showing preferentially corroded CoCrMo grain boundaries and the different grain orientations. (c) CSL boundaries are labeled with red lines, twin boundaries are labeled with black lines, and randomly oriented grain boundaries are labeled with gray lines.

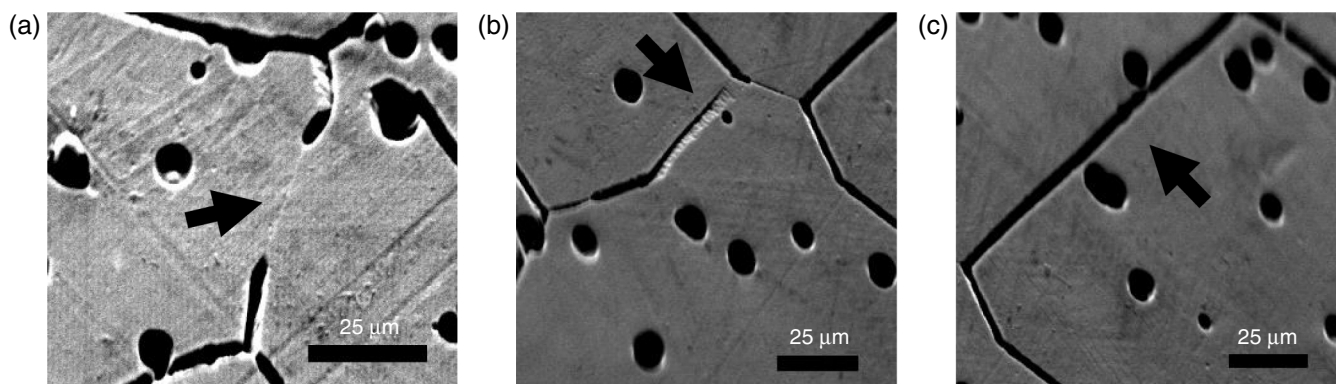


**FIGURE 2.** Representative examples of a (a) Type I, (b) Type II, and (c) Type III grain boundary as indicated by the arrows.

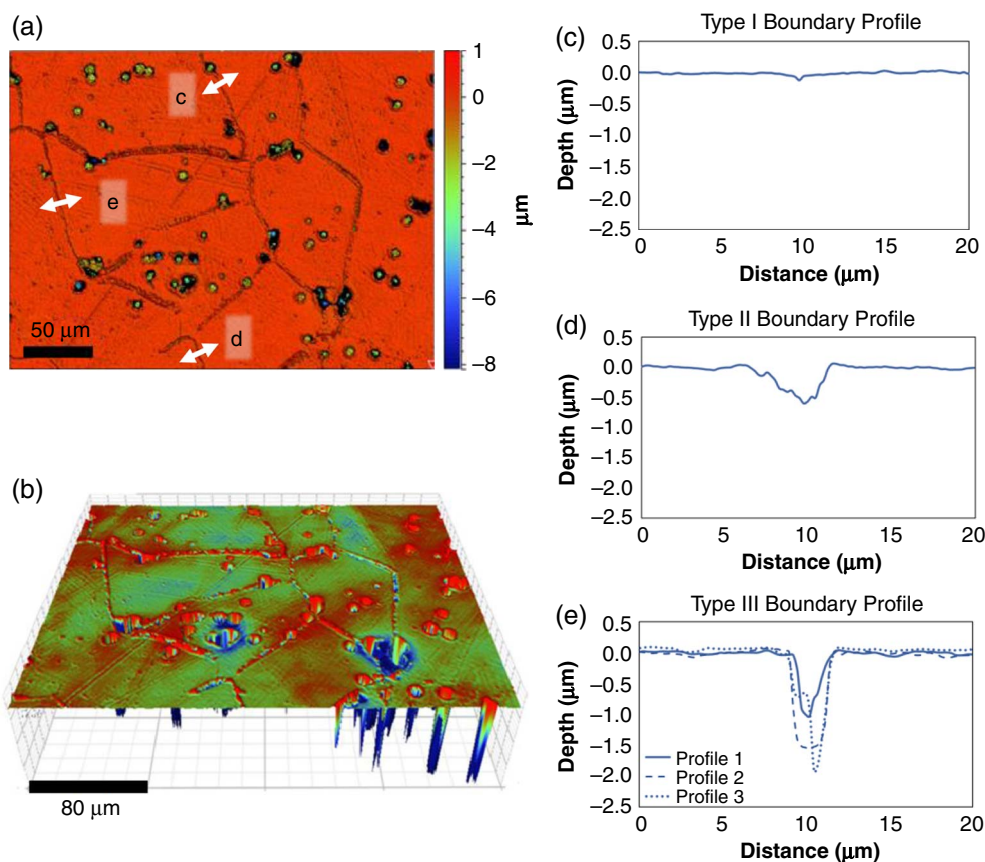


**FIGURE 3.** Profilometry measurements of the same region of interest can be shown as (a) a 2D projection and (b) a 3D reconstruction. Depth profiles of representative (c) Type I, (d) Type II, and (e) Type III boundaries are shown. Type III boundary profiles, taken from 3 different sites along the boundary, show a large variance in the depth measurements.

Figure 3(c), a slight divot formed the Type I boundary, at most corroding to about 0.2  $\mu\text{m}$ . In Figure 3(d), the Type II boundary corroded asymmetrically to a depth of  $\sim 0.6 \mu\text{m}$ . In Figure 3(e), the Type III boundary corroded the deepest, up to  $\sim 2.0 \mu\text{m}$ . This Type III representative example also shows the variety of depths and shapes that were observed along a single corroded Type III boundary.

The grain boundary depth versus  $\Sigma$ -value data are summarized in Figure 4, with the three boundary types indicated on the graph. Corrosion depth served as the measure of corrosion severity. Here, a clear trend between the degree of lattice coincidence and corrosion depth was observed. Type III boundaries had large crevice depth variations, which are designated by the vertical arrows in Figure 3. The arrows shown are not error bars, as they indicate the variation in corrosion depth for single boundaries as a function of position along the boundary.

The width and depth measurements showed an interesting trend. The measurements showed that widths are approximately 2 to 5 times larger than their corresponding depth, as summarized in Figure 5. Type III boundaries generally had lower width to depth ratios, as they corroded down to 3  $\mu\text{m}$ , with widths

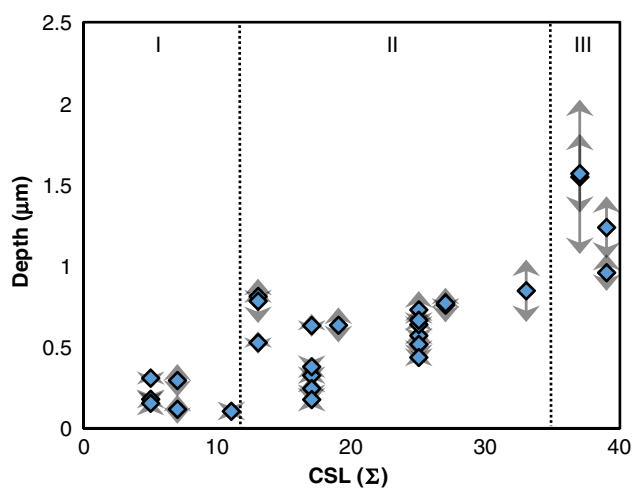


**FIGURE 4.** Corrosion crevice depth was plotted with respect to the CSL  $\Sigma$  number. The three classes of boundaries and their respective corrosion depths are shown.

from 3  $\mu\text{m}$  to 5  $\mu\text{m}$ . Type II boundaries, on the contrary, only corroded to about 1  $\mu\text{m}$ , widths ranging from 2  $\mu\text{m}$  to 5  $\mu\text{m}$ . The width-depth relation showed another

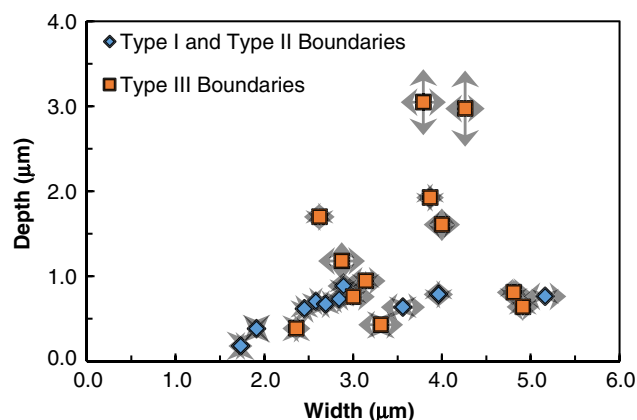


**FIGURE 5.** Crevice measurements collected from 3D profilometry show that widths of the corroded grain boundaries are approximately 2 to 5 times larger than its corresponding depth. The arrows represent the range of measurements along the boundary.

indicative difference between the corrosion behaviors in Types II and III boundaries.

To summarize, the grain boundary types are:

- Type I CSL boundaries with  $\Sigma \leq 11$ . The majority of the boundaries in this class were immune to corrosion, showing no depth of corrosion. Of the boundaries that did corrode, the depth was less than 0.40  $\mu\text{m}$ . These corroded boundaries looked like slight divots.
- Type II CSL boundaries between  $\Sigma 13$  and  $\Sigma 35$ . Many of the CSLs fell within this regime. The crevices were typically asymmetrical and shallower than the general high-angle corrosion boundaries. A total of 31 out of the 57 non-twin CSL boundaries belonged to this class. These corroded boundaries looked like angled wedges.
- Type III Non-CSL boundaries, also known as high-angle grain boundaries. These

boundaries were typically severely corroded with corrosion crevice depths exceeding 1.0  $\mu\text{m}$ . Work focusing on this class of boundaries has been previously described.<sup>16</sup> Boundaries belonging to this class often have large variations in the depth.

### *Effect of Misorientation on Carbide Precipitates*

Previous work on Type III boundaries discussed the carbide morphology and corrosion behavior in detail.<sup>16</sup> Here, the focus is primarily on Type II boundaries, with a brief analysis of two Type I boundaries to follow. Most of the boundaries presented here contained carbide precipitates, and there were two general features of interest observed in the experimental data, namely the precipitate structure and the local segregation around the precipitates.

The precipitate structure is first described, and then this information is connected to the grain boundary energy. Initial TEM imaging of the eight Type II grain boundaries revealed faceting caused by the second phase carbides, with these sensitized boundaries appearing wavy and irregular, as shown in Figure 6. In contrast, one Type II immune boundary was also characterized as being “clean” with no carbides. This immune interface, shown in Figure 7(a), was also almost completely straight. Figures 7(b) and (c) show the diffraction patterns for each grain, with no evidence for carbides along the boundary. For all eight of partially corroded Type II boundaries, chromium-rich carbides were dotted along the grain boundaries. From BF TEM images as shown in Figure 8, nanoscale carbide precipitates of approximately 50 nm to 100 nm in length and 10 nm to 25 nm in width were observed. Most of the chromium-rich carbides observed were lens shaped, showing partial wetting of the grain boundary interface, similar to previous work on Type III boundaries.<sup>16</sup>

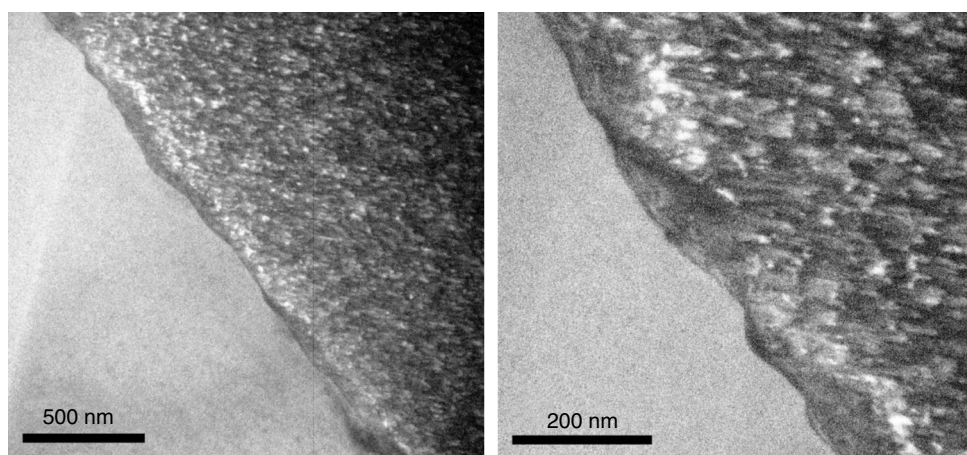


**FIGURE 6.** BF-TEM showed that a partially corroded  $\Sigma 27$  boundary was faceted by carbides.

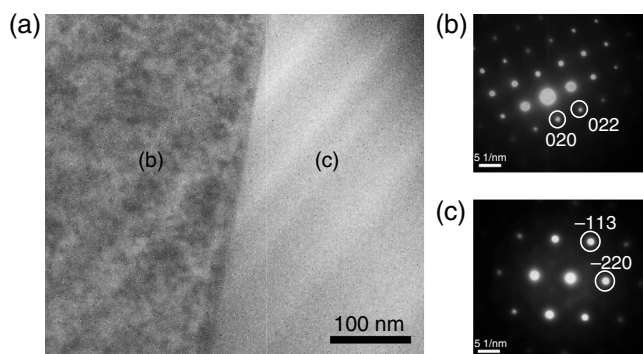


**FIGURE 7.** (a) The immune  $\Sigma 17$  grain boundary was straight without deviations and did not show carbides. (b) and (c) Electron diffraction patterns collected at the adjacent grains confirmed the presence of a grain boundary.

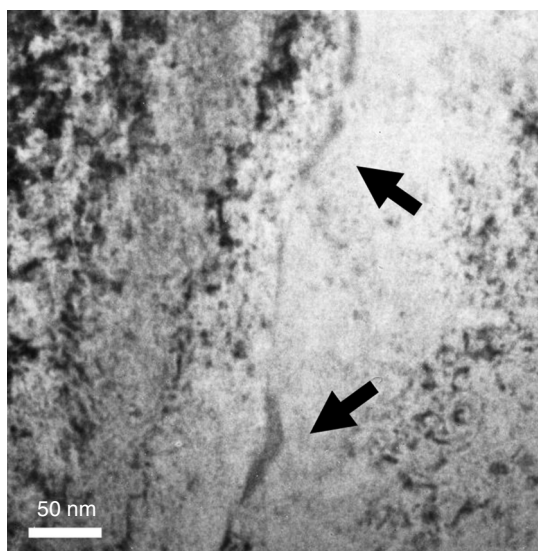


**FIGURE 8.** BF-TEM image of lens-shaped carbides (indicated by arrows) at a partially corroded  $\Sigma 25$  grain boundary.

### High-Angle Annular Dark Field and Energy Dispersive X-Ray Spectroscopy Quantification of Chromium Depletion

The Cr segregation around the grain boundary precipitates is now discussed, along with how this correlated with corrosion susceptibility and the size of the precipitates. The chemical compositions of the Cr depletion zones, specifically the Cr content, were measured using EDS. Figure 9 shows line scans that confirmed the presence of carbides and showed that the carbides were in multiple morphologies. Single and double particles were seen, but Cr depletion was not observed in the immediate vicinity of the carbides.

Further HAADF imaging coupled with EDS maps, which show the spatial variations of the composition, provided additional details of carbides and Cr depletion along Type II grain boundaries. Five HAADF images

with corresponding EDS maps were measured; four representative EDS maps are shown in Figures 10 through 13. Most carbides had the same lens shape as observed in BF-TEM images, shown in Figures 6 and 8. This shape was expected because it was observed in the previous work on Type III boundaries.<sup>16</sup> Figure 10, taken from the same region as Figure 9, is a  $\Sigma 13$  boundary and Figure 11 is a  $\Sigma 25$  boundary. Both of these Type II boundaries showed lens carbides of 50 nm to 100 nm in length and 10 nm to 25 nm in width. Figure 12 shows another  $\Sigma 25$  boundary, this with a different carbide morphology: “platelet”-shaped carbides. In the Type II boundaries, the platelet carbides reached 100 nm in length; however, the maximum widths were only 10 nm. Two of the three  $\Sigma 25$  CSL boundaries analyzed formed platelet-shaped carbides. This links lower corrosion to more coherence between the boundary and the precipitates. Carbides were closer to the “platelet” shape than the lens shape in the low corrosion cases; the platelet-shaped carbides can also be related to the energy of the CSL, which will be addressed later in the discussion.

Of the two Type I boundaries, one was completely immune and the other was a  $\Sigma 7$  boundary that corroded to about 0.3  $\mu\text{m}$ . The immune boundary appeared completely straight and was free of carbides, while the partially corroded boundary, shown in Figure 13, contained small platelet-shaped carbides of about 50 nm in length and 5 nm wide and had no significant effect on grain boundary faceting.

When there were carbides present, Cr depletion zones (CDZs) were observed in the EDS maps. The presence of both  $\text{M}_{23}\text{C}_6$  carbides and CDZs along the grain boundaries was confirmed by comparing the Co-K EDS maps, Cr-K EDS maps, and Mo-L EDS maps. Chemical quantification data from the  $\Sigma 13$  Type II boundary are shown in Figure 10 and are summarized in Table 2. In this Type II boundary, which corroded to 0.8  $\mu\text{m}$ , the area around the carbide contained a CDZ of about 5 at% Cr in between two carbides along the grain boundary. In contrast to the EDS data shown in Figure 9, the improved quality of EDS mapping in Figure 10 revealed the nanoscale CDZ. The area of the CDZ extended about 25 nm, approximately the width of the carbide precipitate, consistent with the previous observations made in Type III boundaries.<sup>16</sup> Additionally, the CDZs formed in all directions from the surface of the precipitates. This observation supports that there was a local “conservation” of Cr in the regions adjacent to the grain boundaries, and that Cr diffusion was also localized.

Less corrosion depth was found to correspond to smaller Cr depletion for a grain boundary. There was a smaller degree of Cr depletion and a smaller area of the CDZ. For  $\Sigma 25$  Type II boundary in Figure 11, which had corroded approximately 0.7  $\mu\text{m}$ , there was a depletion of 4.8 at% in Cr on average, shown by the quantitative EDS measurements in Table 3. In the

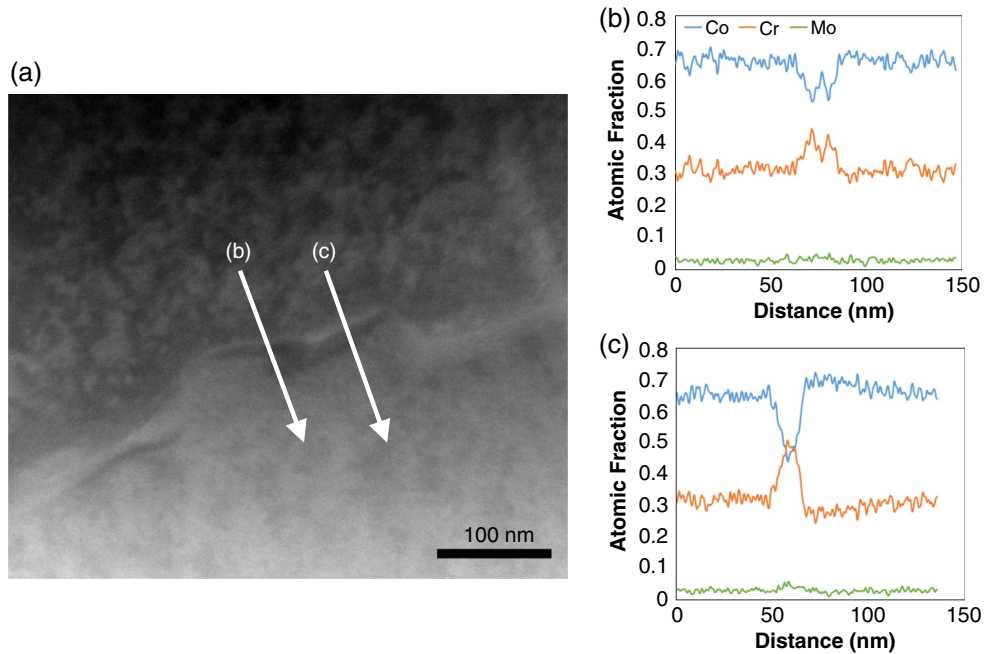


**FIGURE 9.** (a) Two carbides of approximately 100 nm are found along the  $\Sigma 13$  boundary. Line scans from the HAADF image show (b) two peaks representing the two carbides and (c) a single peak showing the Cr content across the center of a carbide.

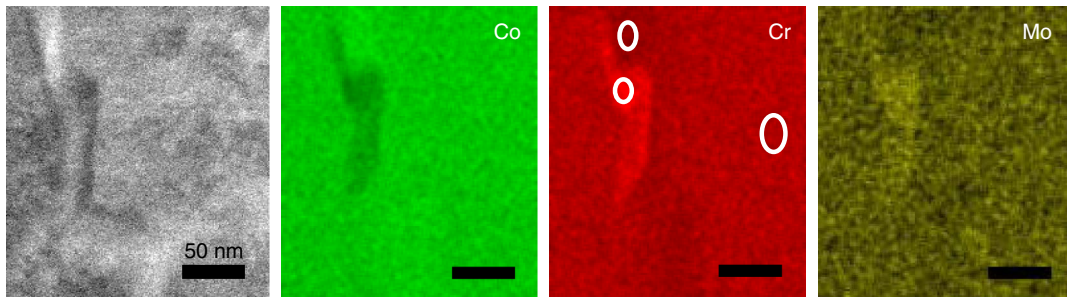


**FIGURE 10.** HAADF image from a corroded  $\Sigma 13$  grain boundary with the corresponding EDS maps as indicated by the rectangle. Chemical quantification from the indicated sites is summarized in Table 2.

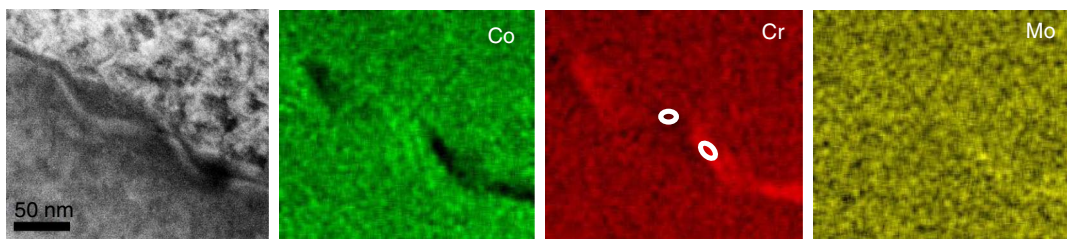


**FIGURE 11.** HAADF image of a corroded  $\Sigma 25$  grain boundary accompanied with the corresponding EDS maps for Co, Cr, and Mo. Cr depletion zones are present in between carbides along the boundary.

lesser corroded  $\Sigma 25$  Type II boundary from Figure 12, which corroded about 0.5  $\mu\text{m}$ , the Cr depletion was approximately 2 at% Cr, with EDS values shown in Table 4. The  $\Sigma 7$  corroded Type I boundary in Figure 13, which corroded to about 0.3  $\mu\text{m}$ , showed levels of Cr depletion of slightly less than 2 at% Cr as

summarized in Table 5. The completely immune Type I boundary contained no appreciable Cr depletion and no carbides were found along the boundary. In addition, the CDZs in Figures 11 through 13 were located in between the carbides and did not form in areas surrounding the precipitates as shown in Figure 10.

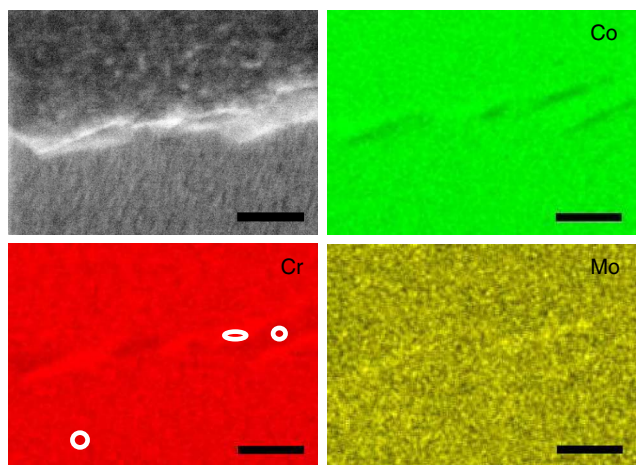


**FIGURE 12.** Platelet-shaped precipitates were found along a  $\Sigma 25$  boundary with low corrosion. The scale bars are 100 nm.

The Cr depletion concentration corresponded well with the depth of corrosion observed at each boundary. The relationship between the level of Cr depletion and the amount of corrosion is summarized in Figure 14, noting the morphology shape as well. Figure 12  $\Sigma 25$  boundary with lower Cr depletion and lower corrosion depth had platelet morphology (similar to the low energy  $\Sigma 7$  boundary). In contrast, Figure 11  $\Sigma 25$  boundary with higher Cr depletion and more corrosion had lens morphology (similar to the higher energy  $\Sigma 13$  boundary).

There was also an enhancement of Mo in the carbide, as shown in the EDS quantification in Tables 3, 4, and 5. However, unlike Cr, there was no consistent reduction of Mo in the CDZ, as the Mo content remained similar to the matrix. Additionally, some of the changes in the Mo concentration, such as in Table 5, were so small that they could not be distinguished from the error associated with the EDS data, which is estimated to be around 1 at%.

In addition to verifying whether the grain boundaries were sensitized, it was also possible to compare the degree of sensitization by comparing the amount of Cr depletion to the matrix and the size of the

**TABLE 2**  
EDS Quantification of Key Regions in Figure 10

	Co (at%)	Cr (at%)	Mo (at%)
Matrix	63.5	32.0	4.5
Carbide	48.1	46.0	5.9
Cr Depletion Zone	69.9	27.3	2.8

**TABLE 3**  
EDS Quantification of Key Regions in Figure 11

	Co (at%)	Cr (at%)	Mo (at%)
Matrix	63.3	32.9	3.8
Carbide	47.1	47.3	5.5
Cr Depletion Zone	69.0	28.3	2.7

**TABLE 4**  
EDS Quantification of Key Regions in Figure 12

	Co (at%)	Cr (at%)	Mo (at%)
Matrix	64.4	31.6	4.0
Carbide	57.4	38.6	4.0
Cr Depletion Zone	68.5	29.4	2.1

**TABLE 5**  
EDS Quantification of Key Regions in Figure 13

	Co (at%)	Cr (at%)	Mo (at%)
Matrix	65.3	31.3	3.4
Carbide	58.6	37.4	4.0
Cr Depletion Zone	66.4	29.9	3.7

CDZs at different CSL boundaries. The degree of the sensitization was linked to the size and shapes of the carbides, suggesting that there was a localized “conservation” of Cr near the precipitates. The structural change of the precipitates from lens shape to platelet shape with different  $\Sigma$ -values were previously noted, which are converted to grain boundary interfacial energy for further analysis in the discussion.

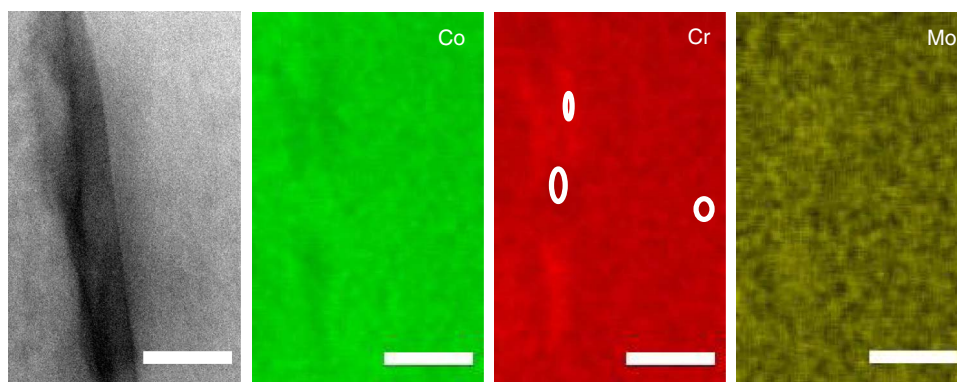


**FIGURE 13.** Platelet-shaped precipitates were also observed in a corroded  $\Sigma 7$  boundary. The scale bars are 50 nm.

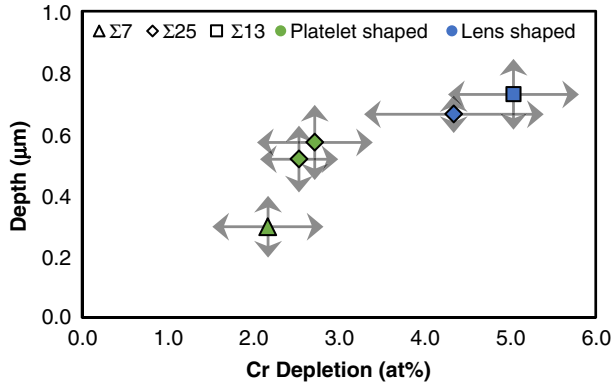


**FIGURE 14.** The Cr depletion at one Type I and four Type II boundaries are related to the susceptibility of corrosion. Note that the energy value for these ranks from lowest to highest as  $\Sigma 5$ ,  $\Sigma 25$ , and  $\Sigma 13$ .

## CORROSION (GACC) MODEL EXPANSION TO TYPE II BOUNDARIES

An explanation of the results is now presented, extending a previously derived model<sup>16</sup> where the sensitization of the grain boundaries is the initiating mechanism of grain boundary assisted crevice corrosion. First, interfacial energies of the experimental CSL values were estimated using previously published molecular dynamic calculations for fcc CSL grain boundaries of pure aluminum, nickel, and copper.<sup>29</sup> While this conversion is not rigorously accurate, it should reflect the general trends. As CoCrMo alloys have a metastable fcc matrix, a scaling factor, determined from the calculated solid state surface energies<sup>30</sup> of the main alloying elements, was applied. The trend of corrosion depth versus interfacial grain boundary energy is shown in Figure 15. The 3D profilometry grain boundary depth measurements indicated that the degree of lattice coincidence is related to the corrosion depth of grain boundaries.

The GACC model for Type III boundaries developed by Hoffman, et al.,<sup>16</sup> can be extended to Type II grain boundaries. This model compares the energy change of corrosion resulting from local Cr depletion to the energy change resulting from removal of the grain boundary, i.e., the grain boundary energy. The difference in composition between the matrix and the Cr depletion region leads to a difference in the corrosion potential that effects the dissolution. Using the EDS data of CDZs from Type II boundaries of varying degrees of corrosion, the average amount of Cr depletion observed in Type II boundaries ranged from 2.2 at% to 5.0 at% Cr, which was below the average 7.1 at% Cr depletion value observed in Type III boundaries.<sup>16</sup> As Cr content decreases, the corrosion potential increases, and the CoCrMo would follow the same trend; the corrosion potential increases 10 mV per 1 at% Cr decreases.<sup>31-32</sup> Following the model, the change in corrosion potential would range from -22 mV to -50 mV. The

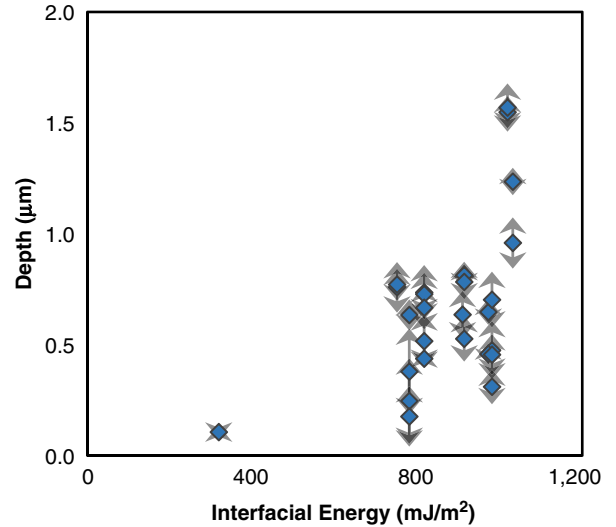


**FIGURE 15.** Interfacial energies associated with different lattice configurations at coincident site lattice (CSL) grain boundaries have been shown to be a good predictor for the severity of corrosion. The arrows in gray represent the range of the measurements observed.

electrochemical difference associated with Cr depletion,  $\Delta\mu$ , was then converted to joules using calculations outlined in the original GACC model.<sup>16</sup>

$$\Delta\mu = \mu_{\text{matrix}} - \mu_{\text{CDZ}} \quad (1)$$

$$\Delta\mu = -22 \text{ mV} \quad \text{to} \quad -50 \text{ mV} \quad (2)$$

$$\Delta\mu = -8.10 \times 10^{-21} \text{ J} \quad \text{to} \quad -1.84 \times 10^{-20} \text{ J} \quad (3)$$

This can be compared to  $-2.61 \times 10^{-20} \text{ J}$  for Type III boundaries, and it is a factor of 1.5 to 3 smaller. Using the same atomic distances for  $a$ , the distance between atoms along the grain boundary, and  $b$ , the distance between atoms perpendicular to the grain boundary, and the CDZ widths  $L$  as described in the original GACC model,  $\Delta E_{\text{CDZ}}$  was calculated, which is the range for energy lost resulting from the CDZ per unit length. The experimental results of Type II boundaries expanded the range of  $\Delta E_{\text{CDZ}}$ .

$$\Delta E_{\text{CDZ}} = \Delta\mu \frac{L}{ab} \quad (4)$$

$$\Delta E_{\text{CDZ}} = -2.77 \times 10^{-7} \frac{\text{mJ}}{\text{m}} \quad \text{to} \quad -12.6 \times 10^{-7} \frac{\text{mJ}}{\text{m}} \quad (5)$$

This compares to  $-3.78 \times 10^{-7}$  to  $-17.9 \times 10^{-7} \text{ mJ/m}$  for Type III boundaries.<sup>16</sup> As calculated in Figure 15, the Type II boundaries examined had  $\gamma_{\text{GB}}$  values ranging between  $780 \text{ mJ/m}^2$  and  $973 \text{ mJ/m}^2$ . By multiplying  $\gamma_{\text{GB}}$  with the weighted average of atomic diameters of Co and Cr (0.382 nm), indicated by  $d$ , the energy of the boundary per unit length was obtained.

$$\Delta E_{GB} = -\gamma_{GB}d \quad (6)$$

$$\Delta E_{GB} = -2.98 \times 10^{-7} \frac{\text{mJ}}{\text{m}} \quad \text{to} \quad -3.72 \times 10^{-7} \frac{\text{mJ}}{\text{m}} \quad (7)$$

This compares to the  $\Delta E_{GB}$  of  $-5.35 \times 10^{-7}$  mJ/m for Type III boundaries;<sup>16</sup> a smaller value of  $-1.53 \times 10^{-7}$  mJ/m was cited in the earlier work, which is for Type I boundaries such as twins (which are immune).

The comparison of  $\Delta E_{CDZ}$  and  $\Delta E_{GB}$  values clearly shows that Type II boundaries fit within the GACC model as both the grain boundary interfacial energy and Cr depletion influenced corrosion sensitivity; neither dominates. The driving force is a factor of 1.5 to 2 smaller than for the Type III boundaries; more comparisons of the different boundaries will be left to the discussion section.

To continue expanding the GACC model, crevice corrosion is considered to further explain the grain boundary crevice shapes that were observed in Type II boundaries. During crevice corrosion, oxygen diffusion is restricted by the small crevice opening and should be largely independent of the type of boundary. The crevice corrosion part of the model is to explain the width-depth relationship. The driving force down the crevice is a result of the CDZ and the width results from the chemistry in the crevice. The model predicts that higher energy Type III non-CSL boundaries would have lower width to depth ratios, and that is indeed what is shown in Figure 5.

## DISCUSSION

Similar to stainless steels, Cr is the main alloying element that provides the corrosion resistance in CoCrMo alloys. The relationship between the level of Cr depletion and the amount of observed corrosion is summarized in Figure 14. All of the observed Cr depletion values fall below the average Cr depletion in Type III boundaries, 7.1 at% Cr.<sup>16</sup> Of the Type II boundaries that were examined, the Cr depletion ranged between 2 at% Cr and 5 at% Cr. Cr at the  $\Sigma 13$  boundary depleted about 5 at% Cr. The average depletion values were between 2 at% Cr to 4.8 at% Cr across the three  $\Sigma 25$  boundaries measured by EDS. In the corroded Type I boundary, a  $\Sigma 7$ , a 1.5 at% Cr depletion was also observed at the boundary. With decreasing grain boundary interfacial energies, there was less Cr depletion at the boundaries because the chromium-rich carbides were smaller and also less enriched in Cr. The Cr depletion is linked to the grain boundary orientation and both play a role in the corrosion susceptibility.

The combination of the Cr depletion and removal of the grain boundary is the initiator of the corrosion, but the real damage to the material (and to a patient with a CoCrMo implant) is from the subsequent crevice corrosion as this leads to a more extensive release of ions. Interestingly, this implies that there may be ways

to mitigate corrosion in vivo by controlling the content of the pseudo-synovial fluid. The fluid concentrations may play a role in variations in the sensitivities of patients which are known to exist, albeit poorly understood; the physiological conditions may vary with age, gender, ethnicity, and other factors.<sup>33-35</sup>

As mentioned earlier, the energies of boundaries are not linear with the  $\Sigma$  value. As verification of this, it is noted that EDS data were collected at four Type II boundaries: for a  $\Sigma 13$  and three  $\Sigma 25$  boundaries. According to the previously discussed method of calculating grain boundary interfacial energies, the  $\Sigma 25$  boundaries have lower energy than  $\Sigma 13$ . By cross referencing back to the profilometry measurements in Figure 5 and graphing with EDS Cr depletion in Figure 14, the three  $\Sigma 25$  boundaries showed lower corrosion depths than the  $\Sigma 13$ . Less Cr depletion at the more stable  $\Sigma 25$  boundaries was also observed. The Type I  $\Sigma 7$  boundary in Figure 14, which has significantly lower energy than  $\Sigma 13$  or  $\Sigma 25$ , has the lowest corrosion depth and Cr depletion.

It was previously noted that a change in carbide morphology was observed along with a decrease in Cr depletion at Type II boundaries with low corrosion, as well as Type I boundaries. Within the  $\Sigma 25$  grain boundaries, both lens-shaped and platelet-shaped carbides were observed. This suggests that there are different energies associated with the  $\Sigma 25$  boundaries. It is necessary to consider grain boundary plane orientation before accounting for deviations from CSL orientations. For example, certain sections of a  $\Sigma 25$  CSL boundary may have a higher density of coincident lattice sites than other sections of much lower  $\Sigma$ -value.<sup>36</sup> It is also possible that boundaries of the same  $\Sigma$ -value have different distributions of coincident lattice points, resulting in different interfacial energies.

Given the experimental results herein, the performance of the alloy can be further optimized with grain boundary engineering. Introducing a larger proportion of geometrically special CSL grain boundaries with thermomechanical processes, strain annealing, or strain recrystallization can potentially reduce localized corrosion at the nanoscale and improve the bulk performance of the alloy. Cahoon, et al.,<sup>37</sup> proposed that applied strain can influence the twin boundary density in pure fcc metals and Cu alloys. Shimada, et al.,<sup>38</sup> demonstrated with stainless steel that a small pre-strain prior to annealing minimized sensitization in electrochemical potentiokinetic reactivation tests and enhanced the frequency of CSL boundaries. It is believed that these processing methods can be extended to CoCrMo alloys. The optimization of thermomechanical treatment parameters to achieve favorable grain boundary character distributions and strong corrosion resistance will be critical for the realization of higher performance CoCrMo alloys.

Finally, it is noted that under the conditions of the electrochemical testing, Cr ions, sodium,

potassium, chlorine, and proteins were present in the crevice. As a bovine calf serum solution buffered with phosphate-buffered saline was used to simulate physiological conditions in vivo, other components such as vitamins, growth factors, amino acids, and hormones were present, causing the system to be complex in comparison to standard corrosion testing etchants. This environment causes complex corrosion that can be difficult to completely capture in a model and leaves open many further studies—particularly if one considers the different in vivo physiological conditions.

## CONCLUSIONS

- ❖ Three-dimensional profilometry showed that crevice widths are 2 to 5 times larger than the crevice depths, with Type II boundaries falling closer the upper threshold of this range.
- ❖ Nanoscale chromium-rich carbides and Cr depletion zones were observed in Type II boundaries. With decreasing Cr depletion and grain boundary interfacial energy, the carbides were platelet shaped instead of lens shaped.
- ❖ Type II boundaries, defined to be CSL boundaries between  $\Sigma 13$  and  $\Sigma 35$ , corroded less than 1.0  $\mu\text{m}$  in depth. The average depletion ranged between 2 at% Cr and 5 at% Cr, which influenced corrosion susceptibility.

## ACKNOWLEDGMENTS

We thank Pooja Panigrahi for the samples used in this study, and ATI Allvac for the donation of the alloy materials. AL was assisted by grants from the Undergraduate Research Grant Program which is administered by Northwestern University's Office of Undergraduate Research. EEH was supported by the Department of Defense (DoD) through the National Defense Science and Engineering Graduate Fellowship (NDSEG) program. This research was funded by the National Science Foundation on grant number CMMI-1030703.

## REFERENCES

1. M.L. Wolford, K. Palso, A. Bercovitz, *NCHS Data Brief* 186 (2015): p. 1-8.
2. B. Bashinskaya, R.M. Zimmerman, B.P. Walcott, V. Antoci, *ISRN Orthop.* 2012 (2012): p. 8.
3. S.A. Jacobsson, K. Djerf, O. Wahlstrom, *Clin. Orthop. Relat. Res.* 329 (1996): p. S60-S68.
4. S. Pramanik, A.K. Agarwal, K.N. Rai, *Trends Biomater. Artif. Organs* 19, 1 (2005): p. 15-26.
5. I. Milosev, M. Remskar, *J. Biomed. Mater. Res. A* 91, 4 (2009): p. 1100-1110.
6. A.J. Hart, P.D. Quinn, B. Sampson, A. Sandison, K.D. Atkinson, J.A. Skinner, J.J. Powell, J.F. Mosselmans, *Acta Biomater.* 6, 11 (2010): p. 4439-4446.
7. L.D. Dorr, Z.I. Wang, D.B. Longjohn, B. Dubois, R. Murken, *J. Bone Joint Surg.-Am.* 82A, 6 (2000): p. 789-798.
8. C.P. Delaunay, F. Bonnomet, P. Clavert, P. Laffargue, H. Migaud, *Clin. Orthop. Relat. Res.* 466, 2 (2008): p. 340-346.
9. E. Bain, R. Aborn, J. Rutherford, *Trans. Am. Soc. Steel Treat.* 21, 1 (1933): p. 481-509.
10. E. Smethurst, R.B. Waterhouse, *J. Mater. Sci.* 12, 9 (1977): p. 1781-1792.
11. H.E. Placko, S.A. Brown, J.H. Payer, *J. Biomed. Mater. Res.* 39, 2 (1998): p. 292-299.
12. C. Stawstrom, M. Hillert, *J. Iron Steel Inst.* 207 (1969): p. 77-89.
13. S.M. Bruemmer, L.A. Charlot, *Scrip. Metall.* 20, 7 (1986): p. 1019-1024.
14. C.S. Pande, M. Suenaga, B. Vyas, H.S. Isaacs, D.F. Harling, *Scrip. Metall.* 11, 8 (1977): p. 681-684.
15. S.M. Bruemmer, B.W. Arey, L.A. Charlot, *Corrosion* 48, 1 (1992): p. 42-49.
16. E.E. Hoffman, A. Lin, Y. Liao, L.D. Marks, *Corrosion* 72, 11 (2016): p. 1445-1461.
17. C. Montero-Ocampo, E.L. Martínez, *ECS Trans.* 19, 33 (2009): p. 37-48.
18. Y. Liao, R. Pourzal, P. Stemmer, M.A. Wimmer, J.J. Jacobs, A. Fischer, L.D. Marks, *J. Mech. Behav. Biomed. Mater.* 12 (2012): p. 39-49.
19. E. Bettini, T. Eriksson, M. Boström, C. Leygraf, J. Pan, *Electrochim. Acta* 56, 25 (2011): p. 9413-9419.
20. T. Watanabe, S. Tsurekawa, *Acta Mater.* 47, 15-16 (1999): p. 4171-4185.
21. G. Palumbo, K.T. Aust, *Acta Metall. Mater.* 38, 11 (1990): p. 2343-2352.
22. P. Lin, G. Palumbo, U. Erb, K.T. Aust, *Scrip. Metall. Mater.* 33, 9 (1995): p. 1387-1392.
23. E.M. Lehecky, A.M. Brennenstuhl, I. Thompson, *Corros. Sci.* 46, 10 (2004): p. 2383-2404.
24. Y. Pan, B.L. Adams, T. Olson, N. Panayotou, *Acta Mater.* 44, 12 (1996): p. 4685-4695.
25. T. Watanabe, *J. Phys. Colloques* 46, C4 (1985): p. 555-566.
26. H.W. Liu, M. Gao, D.G. Harlow, R.P. Wei, *Scrip. Metall. Mater.* 32, 11 (1995): p. 1807-1812.
27. P. Panigrahi, Y. Liao, M.T. Mathew, A. Fischer, M.A. Wimmer, J.J. Jacobs, L.D. Marks, *J. Biomed. Mater. Res. B* 102, 4 (2014): p. 850-859.
28. D.G. Brandon, *Acta Metall.* 14, 11 (1966): p. 1479-1484.
29. P.R.M. van Beers, V.G. Kouznetsova, M.G.D. Geers, M.A. Tschopp, D.L. McDowell, *Acta Mater.* 82 (2015): p. 513-529.
30. Y. Shibuta, S. Takamoto, T. Suzuki, *Comput. Mater. Sci.* 44, 4 (2009): p. 1025-1029.
31. W.K. Kelly, R.N. Iyer, H.W. Pickering, *J. Electrochem. Soc.* 140, 11 (1993): p. 3134-3140.
32. R. Frankenthal, H. Pickering, *J. Electrochem. Soc.* 120, 1 (1973): p. 23-26.
33. Y. Nakayama, T. Narita, A. Mori, S. Uesaka, K. Miyazaki, H. Ito, *Arthritis Rheum.* 46, 8 (2002): p. 2105-2108.
34. J.M. Jordan, G. Luta, T. Stabler, J.B. Renner, A.D. Dragomir, V. Vilim, M.C. Hochberg, C.G. Helmick, V.B. Kraus, *Arthritis Rheum.* 48, 3 (2003): p. 675-681.
35. M. Maleki-Fischbach, J.M. Jordan, *Arthritis Res. Ther.* 12, 4 (2010): p. 1.
36. D.H. Warrington, P. Bufalini, *Scrip. Metall.* 5, 9 (1971): p. 771-776.
37. J.R. Cahoon, Q.Y. Li, N.L. Richards, *Mater. Sci. Eng. A* 526, 1-2 (2009): p. 56-61.
38. M. Shimada, H. Kokawa, Z.J. Wang, Y.S. Sato, I. Karibe, *Acta Mater.* 50, 9 (2002): p. 2331-2341.